APPENDIX C: SIMULATIONS

In order to check that the detected planetary signal does not come from the filtering process, we conducted simulations to test our three methods on two different data sets: one where the presence of a planet was input in the simulation (scenario #1), and one without any planet (scenario #2). Stokes *I* and *V* LSD profiles were generated from the brightness and magnetic maps found in Sec. 4, at the same dates of observation as the real data, with a comparable noise level. The added planet signature had the properties of the best fit found with the second method (Sec. 5.2): K=0.154 km s^{-1}, $P_{\rm orb}/P_{\rm rot}$=15.29, ϕ=0.671. Applying ZDI to these data sets, we reconstructed brightness and magnetic maps as in Sec. 4. For both simulations, the maps we found look similar to the ones reconstructed from the real data, with an information loss amounting to 4% for the spottedness and ≃80 G for the rms magnetic flux, but the main features, such as the polar spot, are recovered. Fig. C1 shows the brightness maps for simulation #1, at both epochs.

As in Sec. 5.1, synthetic RV curves are shown in Fig. C2, C3 for simulations #1 and #2 respectively. While a signal is detected in the filtered RVs of simulation #1 (rms 107 m s^{-1}), no significant signal is detected in the filtered RVs in simulation #2 (rms 58 m s^{-1}). Table C1 summarises the characteristics of the best fit to the filtered RVs for both scenarii, in comparison with a (K=0 km s^{-1}, RV$_0$=0 km s^{-1}) curve. The periodograms of the filtered RV curves, displayed in Fig. C4 and Fig. C5, further confirm this, with simulation #2 yielding no significant signal at the frequencies found with our three methods in Sec. 5.

We note that changing the noise pattern can make the FAP of the filtered RVs highest peak vary between 4% and 26% for simulation #2 (no planet). It can also change the relative power of the different orbital periods in the filtered RVs for simulation #1: most of the time the ≃10.8 d period is recovered as the highest peak with a FAP<0.5%, but the ≃9.0 d period reaches a smaller $\chi^2_{\rm r}$ in one case out of five. This sheds light on why the different methods do not always favour the same orbital periods in our analysis.

The second method also recovers the different orbital periods from simulation #1, the ≃10.8 d one being the most likely, with a $\Delta\chi^2$ of 7.37 compared to the ≃13.4 d period and 7.67 compared to the ≃9.0 d period. Fig. C6 shows the $\chi^2_{\rm r}$ map around the minimum $P_{\rm orb}$≃10.8 d for ϕ=0.67 (value at the 3-D local minimum), with the white colour bounding the 99.99% confidence region. We chose not to apply this method on simulation #2 (without planet) because it runs computations for orbital parameters close to the local minima found with the first method, and no such significant minima were found for simulation #2.

GPR also successfully recovers the input planet period in simulation #1, as shown in Fig. C7 on which the raw RVs, the planet signal and the residual RVs at $P_{\rm orb}$=15.31$P_{\rm rot}$

Scenario #1	Scenario #2
K=0.122±0.020 km s^{-1} $P_{\rm orb}/P_{\rm rot}$=15.35±0.16 ϕ=0.647±0.026 RV$_0$=0.018±0.014 km s^{-1} $\chi^2_{\rm r}$=0.540	K=0.036±0.021 km s^{-1} $\chi^2_{\rm r}$=0.436
K=0 km s^{-1} $\chi^2_{\rm r}$=1.893	K=0 km s^{-1} $\chi^2_{\rm r}$=0.529
$\Delta\chi^2$=39.2 $\Delta(\log \mathcal{L}_r)$=-16.57	$\Delta\chi^2$=2.7 $\Delta(\log \mathcal{L}_r)$=-0.49

Table C1. Results found with the 1st method on both simulation datasets. The first column shows the results on the scenario with a planet and the second column shows the results on the scenario without planet. For each, a comparison is made between the best sine fit to the filtered RVs and a fit by a constant value, with the reflex motion semi-amplitude K, the orbital period $P_{\rm orb}$ in units of $P_{\rm rot}$, the phase of inferior conjunction ϕ relative to cycle 11.0, the mean RV RV$_0$ and $\chi^2_{\rm r}$. Differences in χ^2 (summed on 29 data points) and in logarithmic ($\log_e$) likelihood are given in the last row.

Scenario #1
K=0.155±0.022 km s^{-1} $P_{\rm orb}/P_{\rm rot}$=15.32±0.14 ϕ=0.662±0.036 $\chi^2_{\rm r}$=0.95226
K=0 km s^{-1} $\chi^2_{\rm r}$=0.97529
$\Delta\chi^2$=30.0 $\Delta(\log \mathcal{L}_r)$=-10

Table C2. Characteristics of the best fit found with the 2nd method on simulation #1 (top row), compared to a fit with a no-planet model (i.e. K=0 km s^{-1}, middle row). Differences in χ^2 (summed on 2581 data points) and in logarithmic ($\log_e$) likelihood are given in the last row.

Scenario #1	Scenario #2
K=0.138±0.027 km s^{-1} $P_{\rm orb}/P_{\rm rot}$=15.31±0.21 ϕ=0.646±0.038 θ_1=1.14±0.21 km s^{-1} θ_2=1.0002±0.0002 $P_{\rm rot}$ log $\mathcal{L}_r$=-6.20	K=0.060±0.052 km s^{-1} log $\mathcal{L}_r$=-5.99
K=0 km s^{-1} log $\mathcal{L}_r$=-21.42	K=0 km s^{-1} log $\mathcal{L}_r$=-5.48
Δ(log $\mathcal{L}_r$)=-15.22	Δ(log $\mathcal{L}_r$)=-0.51

Table C3. Characteristics of the best fit (first row) found with the 3rd method on simulation #1 (left) and #2 (right), compared to a fit with a no-planet model (i.e. K=0 km s^{-1}, middle row). Differences in logarithmic (log$_e$) likelihood are given in the last row.

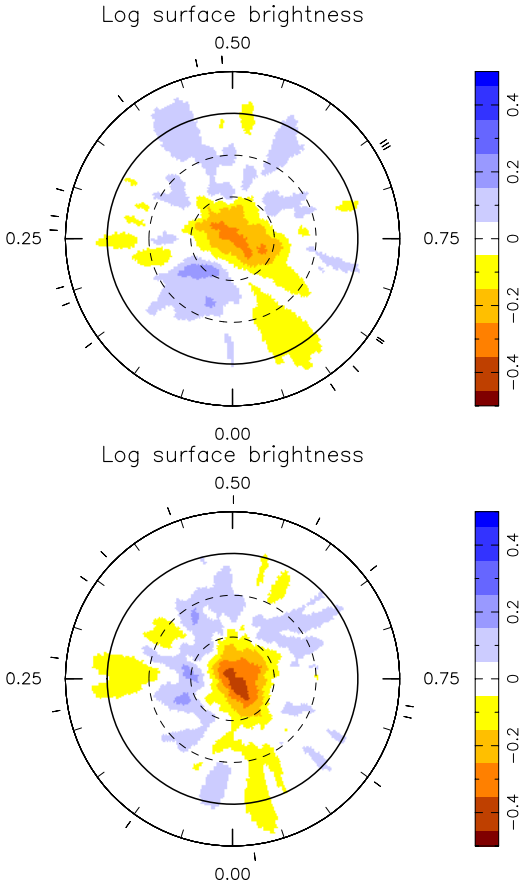

Figure C1. Brightness maps reconstructed from the simulation #1 data, for the 2015 Nov data subset (top) and the 2016 Jan data subset (bottom). Both maps feature a spot coverage of ≃8%.

are seen. The results of the MCMC runs are shown in the phase plots of Fig. C8 and C9, demonstrating that no orbital period stands out in simulation #2, i.e., in the activity jitter synthesised from the reconstructed brightness maps, whereas several orbital periods are detected in simulation #1, ≃10.8 d and ≃9.0 d being respectively the most likely and the second most likely, with a Bayes factor of only 1.25 between them. The comparison with a MCMC run where no planet is subtracted is shown in table C3 for both scenarii, demonstrating that, for scenario #1, taking a planet into account in the model results in a significant increase in the likelihood of the best fit, whereas it is not the case for scenario #2.

We conclude that all three methods enable us to recover the planet signal (scenario #1), and that the detected periods in the observational filtered RVs are not artifacts of the numerical process (scenario #2). Furthermore, for our particular observation window, the noise pattern can change the relative likelihood of the different detected peaks, as can the choice of the method to use.

This paper has been typeset from a TEX/LATEX file prepared by the author.

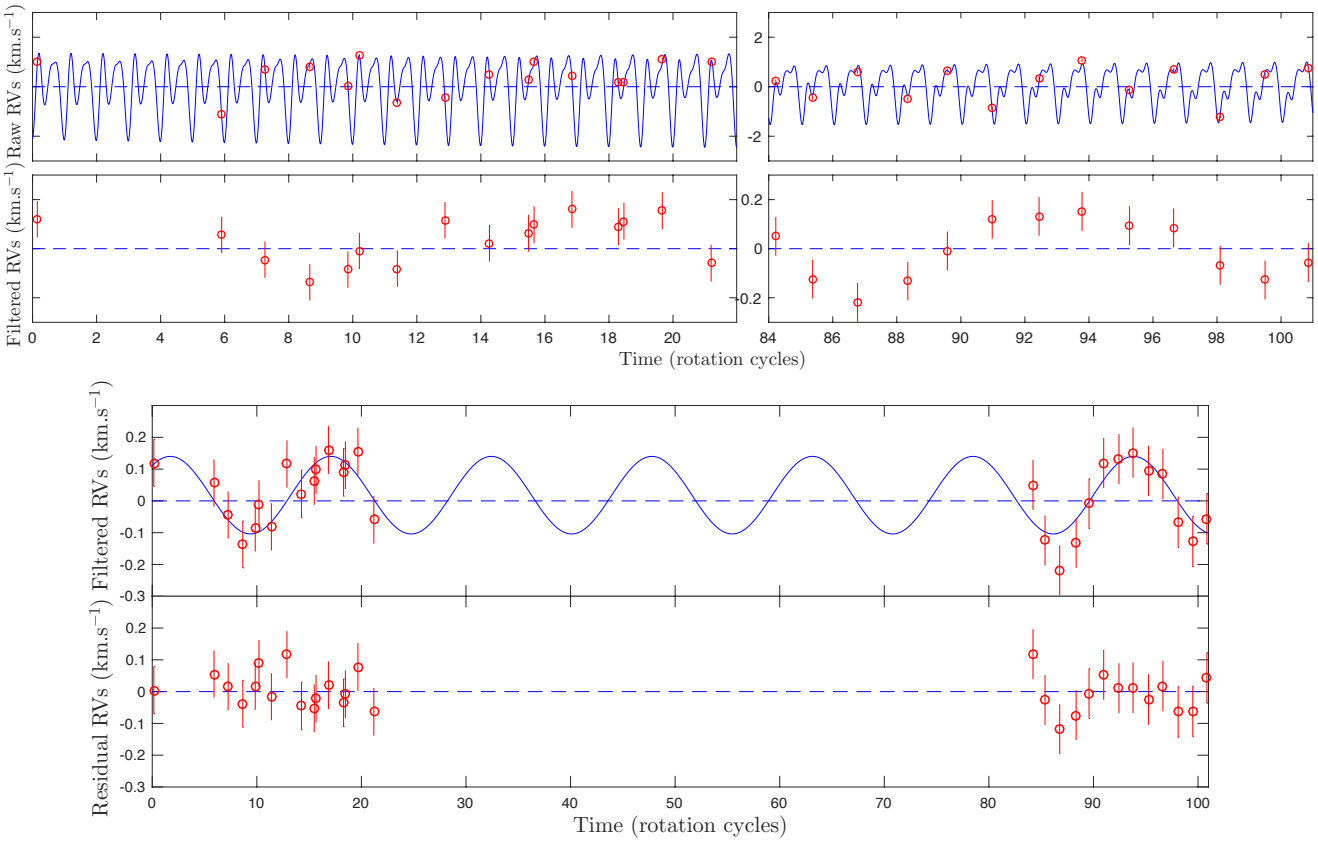

Figure C2. Simulation #1: raw, filtered and residual RV curves as derived with the method described in 5.1. The residual RVs feature a rms value of 59 m s^{-1}.

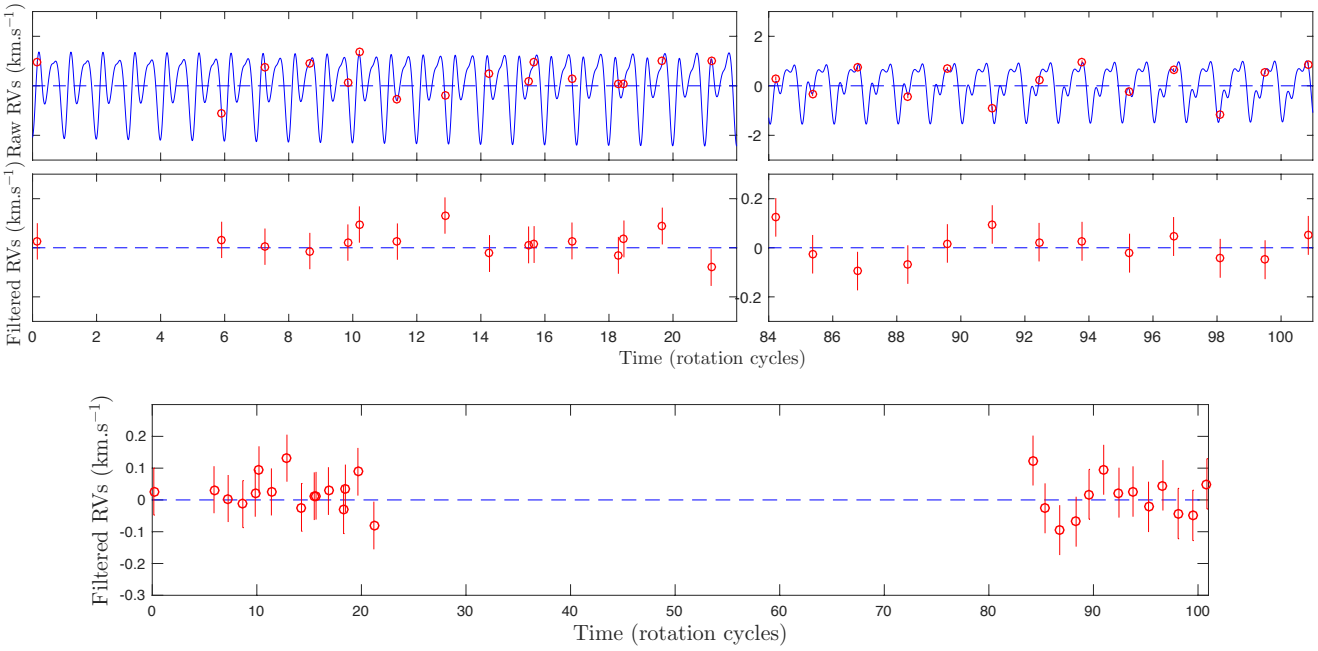

Figure C3. Simulation #2: raw and filtered RV curves as derived with the method described in 5.1. The filtered RVs feature a rms value of 58 m s^{-1}.

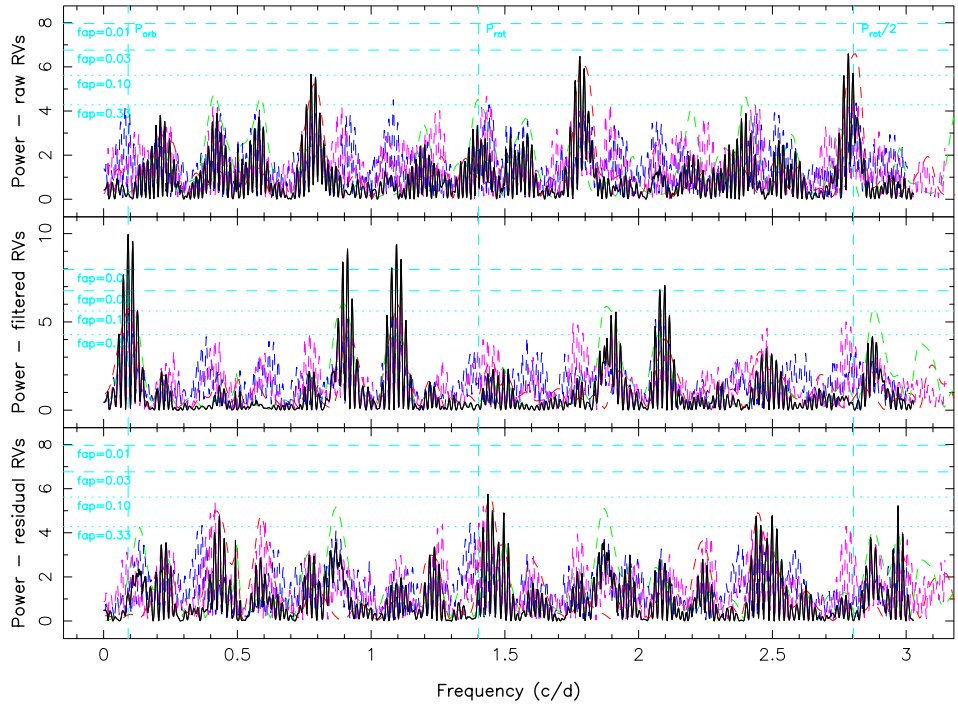

Figure C4. Simulation #1: periodograms of the raw (top), filtered (middle) and residual (bottom) RVs.

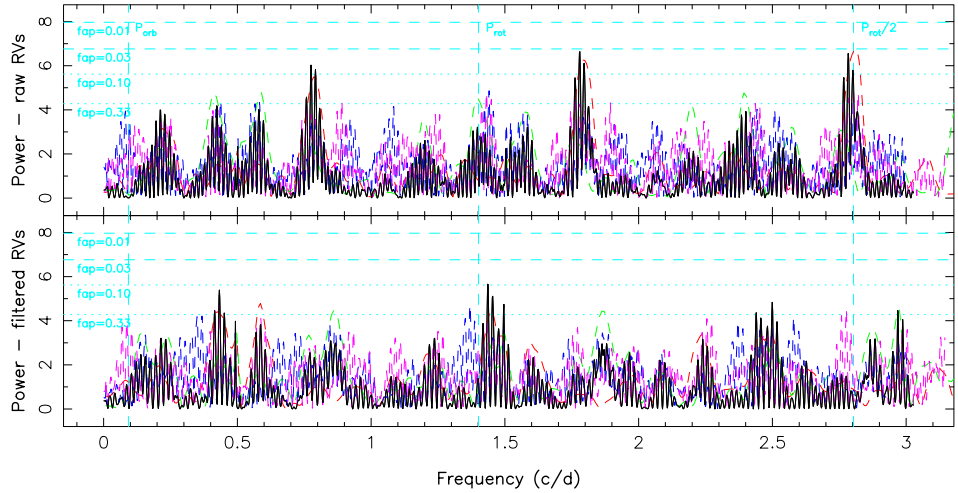

Figure C5. Simulation #2: periodograms of the raw (top) and filtered (bottom) RVs.

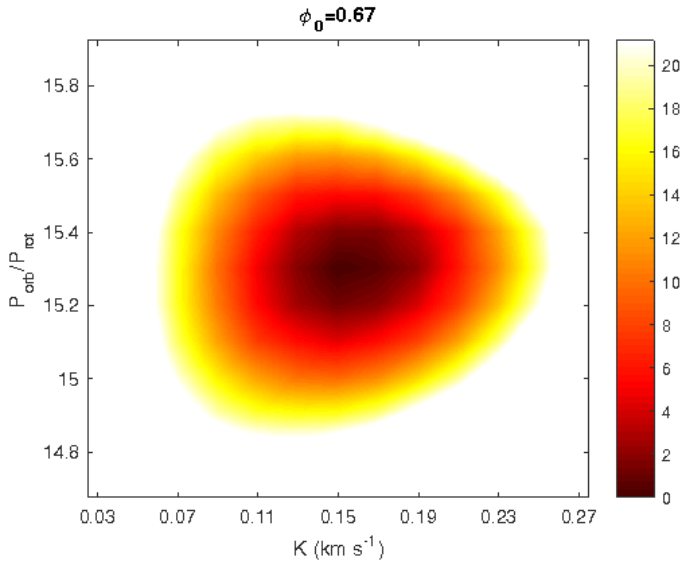

Figure C6. Simulation #1: $\Delta\chi^2$ map at ϕ=0.67 as derived with the method described in 5.2, centered around the minimum $P_{\rm orb}$=15.3 $P_{\rm rot}$. Parameters values are found to be K=0.155±0.022 km s^{-1}, $P_{\rm orb}$=15.32±0.14 $P_{\rm rot}$. The minimum value of $\chi^2_{\rm r}$ is 0.95226

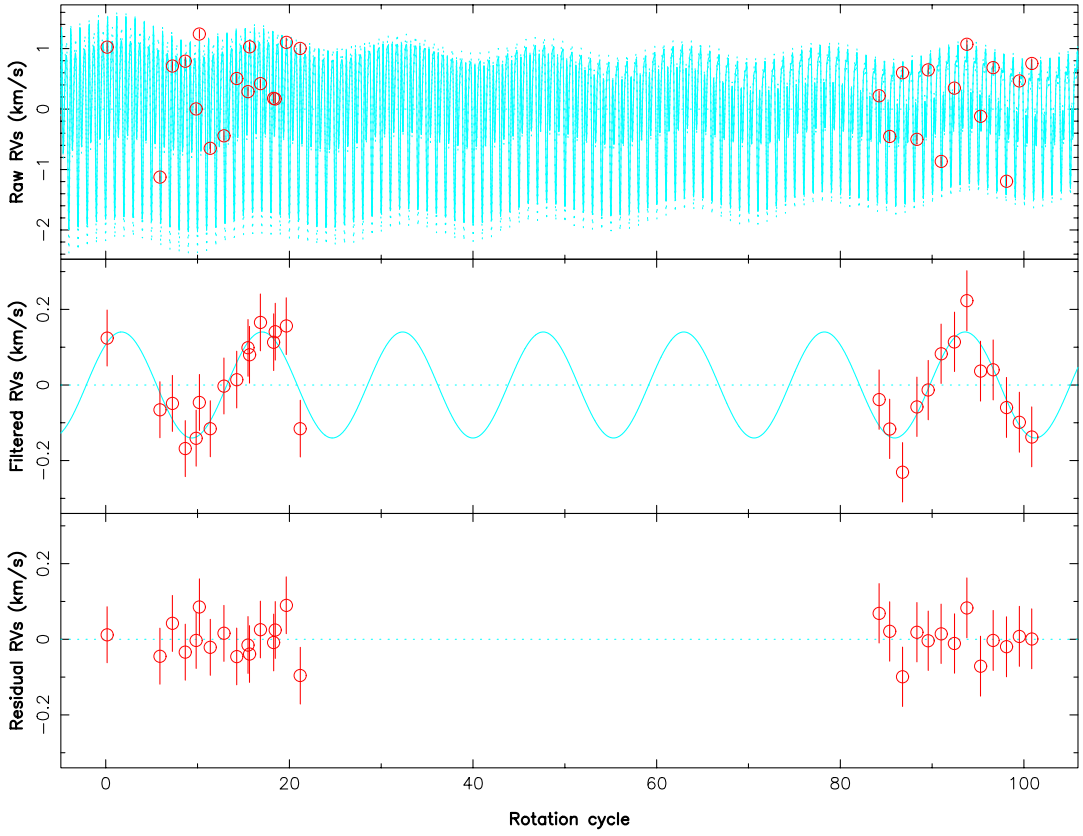

Figure C7. Example of GPR for simulation #1. Top: raw RVs (red dots) and GP fit+planet (cyan), middle: curves as derived with the method described in 5.3, for the local minimum $P_{\rm orb}$=15.31±0.21 $P_{\rm rot}$, K=0.138±0.027, ϕ=0.646±0.038,. The rms of the residual RVs amounts to 47 m s^{-1}.

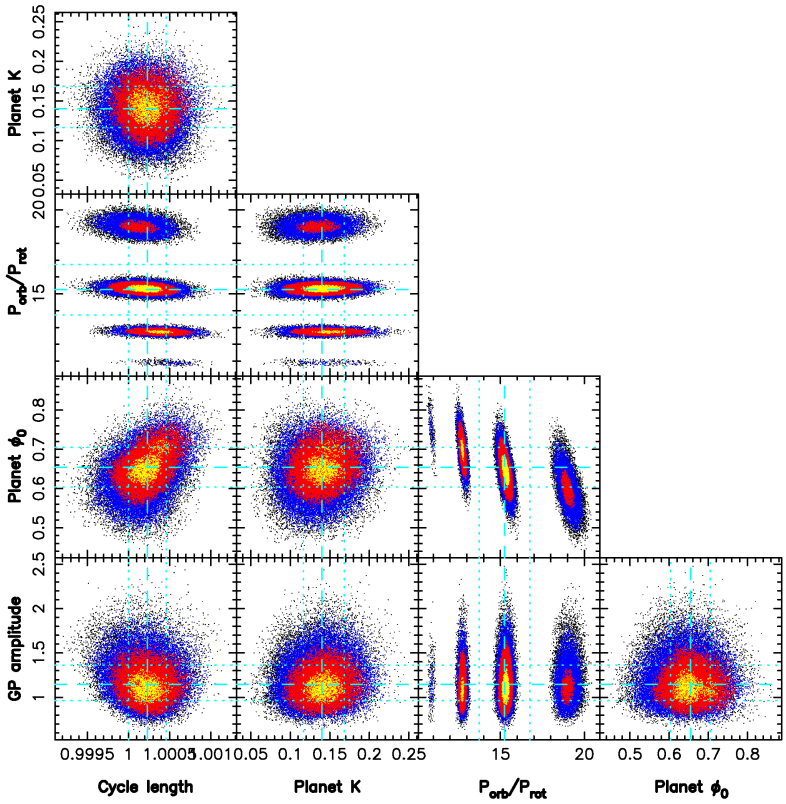

Figure C8. Simulation #1: phase plots of the MCMC run as described in 5.3. We find θ_1=1.15±0.19 km s^{-1}, θ_2=1.0002±0.0002 $P_{\rm rot}$, K=0.140±0.026 km s^{-1}, and the dominant orbital periods $P_{\rm orb}$=15.31±0.21 $P_{\rm rot}$ and $P_{\rm orb}$=12.74±0.13 $P_{\rm rot}$, with the corresponding phases being ϕ=0.646±0.038 and ϕ=0.699±0.036 respectively.

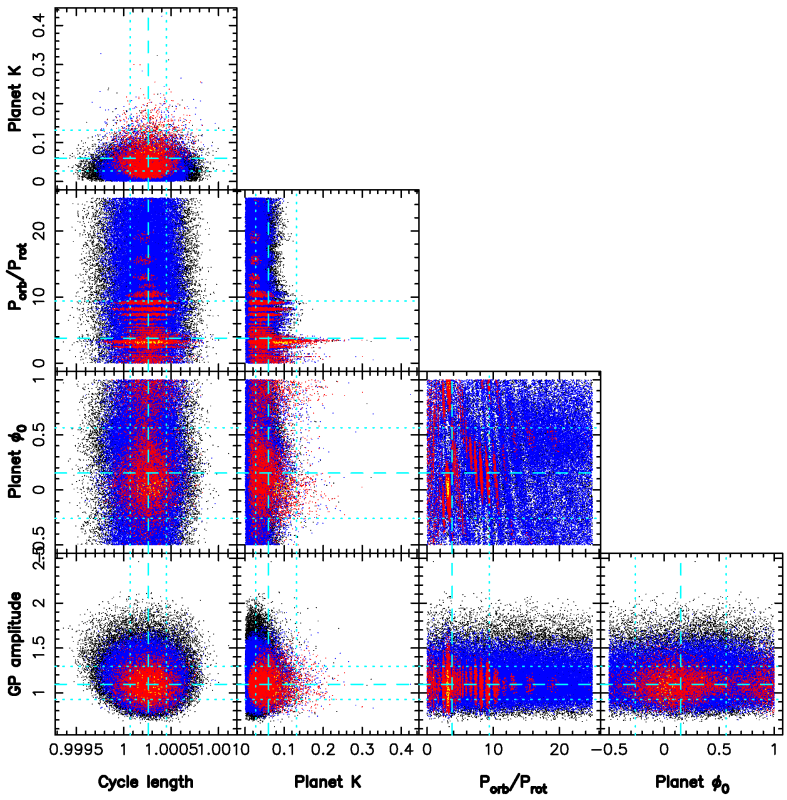

Figure C9. Simulation #2: phase plots of the MCMC run as described in 5.3. We find θ_1=1.09±0.19 km s^{-1}, θ_2=1.0003±0.0002 $P_{\rm rot}$ and K=0.060±0.053 km s^{-1}.